Communications Earth & Environment https://doi.org/10.1038/s43247-026-03227-2

Article in Press

Igneous and sedimentary origins of Jezero crater units from X-ray crystal mapping on Mars

Received: 2 May 2025

Accepted: 16 January 2026

Cite this article as: Orenstein, B.J., Flannery, D.T., Jones, M.W. *et al.* Igneous and sedimentary origins of Jezero crater units from X-ray crystal mapping on Mars. *Commun Earth Environ* (2026). https://doi.org/10.1038/s43247-026-03227-2

Brendan J. Orenstein, David T. Flannery, Michael W. M. Jones, Eleanor L. Moreland, Kirsten L. Siebach, Michael M. Tice, Allan H. Treiman, Briony Horgan, Balz Kamber, Athanasios Klidaras, Luke Nothdurft, Yang Liu, Edward A. Cloutis, Abigail C. Allwood & Scott VanBommel

Igneous and sedimentary origins of Jezero crater units from X-ray crystal mapping on Mars

Brendan J. Orenstein [a, b], David T. Flannery [a*, b], Michael W. M. Jones [b, c, d], Eleanor L. Moreland [e], Kirsten L. Siebach [e], Michael M. Tice [f], Allan H. Treiman [g], Briony Horgan [h], Balz Kamber [a], Athanasios Klidaras [h], Luke Nothdurft [a, b], Yang Liu [i], Edward A. Cloutis [j], Abigail C. Allwood [i], Scott VanBommel [k]

[a] School of Earth and Atmospheric Sciences, Queensland University of Technology, Brisbane, QLD 4000, Australia.

[b] Centre for Planetary Surface Exploration, Queensland University of Technology, Brisbane, QLD 4000, Australia.

[c] Central Analytical Research Facility, Queensland University of Technology, Brisbane, QLD 4000, Australia.

[d] School of Chemistry and Physics, Queensland University of Technology, Brisbane, QLD 4000, Australia.

[e] Department of Earth, Environmental and Planetary Sciences, Rice University, Houston, TX 77005, USA.

[f] Department of Geology and Geophysics, Texas A&M University, College Station, TX 77843, USA.

[g] Lunar and Planetary Institute, Universities Space Research Association, Houston, TX 77058, USA.

[h] Department of Earth, Atmospheric, and Planetary Sciences, Purdue University, West Lafayette, IN 47907, USA.

[i] Jet Propulsion Laboratory, California Institute of Technology, Pasadena, CA 91109, USA.

[j] Department of Geography, University of Winnipeg, Winnipeg, MB R3B 2E9, Canada.

[k] Department of Earth, Environmental and Planetary Sciences, Washington University in St. Louis, St. Louis, MO 63130, USA.

Abstract

Jezero crater is located in Mars' largest olivine-rich region, which is variously interpreted as lava flows, intrusive plutons, clastic sediments, or pyroclastics. In Jezero crater, a variety of olivine-rich units have been investigated by the *Perseverance* rover, including an olivine cumulate in the crater floor (Séítah formation) and the enigmatic "Margin Unit"; an olivine- and carbonate-rich unit commonly interpreted as either a lake shore deposit or a local expression of the regional olivine-carbonate unit. We developed a method to accurately determine the forsterite content (molar percentage of $MgO/(MgO+FeO_T)$) of monocrystalline olivine encountered by *Perseverance*. Forsterite content of monocrystalline olivine in clastic sediments of the western Jezero fan indicate multiple olivine sources. In contrast, monocrystalline olivine analysed in the Margin Unit is similar to the Séítah formation, however, with a slightly greater spread in forsterite content. Our results suggest that at least some of the Margin Unit may represent an altered igneous cumulate with similar origins to the Séítah formation.

Main

The southwestern rim of the ~3.96 Ga[1] Isidis Planitia impact basin and the Nili Fossae area hosts one of the most expansive olivine-rich deposits on Mars[2,3] (Fig. S1). This area is also unique for preserving regionally-extensive magnesium carbonate and large (mm-sized) olivine grains[3,4]. The olivine has been attributed to impact-related melting/intrusive volcanism[2,5,6], lava flows[3,7], clastic sedimentary[8] and/or explosive volcanic processes[9,10], with carbonate addition via hydrothermal alteration or surface weathering of mafic minerals[4,11-14] and possibly with a contribution from direct precipitation of carbonate in ephemeral lakes[15].

Since the Mars 2020 *Perseverance* rover landed in Jezero crater in 2021, it has traversed, analysed, and sampled olivine in aqueously altered igneous rocks in the crater floor (Séítah and Máaz formations), in clastic rocks in the fan cropping out on the western edge of the crater (Tenby and Otis Peak formations), and in enigmatic rocks outcropping along the western margin of the crater (the Margin Unit). Elemental chemistry measurements have been performed by SuperCam via Laser Induced Breakdown Spectroscopy (LIBS)[16,17], as well as by the Planetary Instrument for X-ray Lithochemistry (PIXL); a micro-X-ray fluorescence (XRF) spectrometer mounted to *Perseverance's* robotic arm[18]. Fluoresced X-rays detected by PIXL are used to

generate quantitative elemental abundance maps, typically of cm-sized regions exposed by the rover's abrasion tool[19]. X-ray diffraction peaks are also present in PIXL's XRF spectra[20,21], allowing PIXL to acquire co-located elemental and crystallographic information[20,22-26]. PIXL data can be co-registered with images for expanded spatial context, such as the PIXL Micro-Context Camera (MCC)[18], close up images from the Wide Angle Topographic Sensor for Operations and eNgineering (WATSON), and Autofocus Context Imager (ACI) cameras mounted to the rover's robotic arm[27]. Additional context is provided by navigation cameras (Navcam) and hazard avoidance cameras (Hazcam)[28].

Olivine fosterite content (Fo-content, defined here as the molar percentage of $MgO/(MgO+FeO_T)$) is a useful indicator of the magnesium to iron ratio in melts[29] and therefore clast provenance[30]. However, inaccurate mineral quantifications can occur due to contributions from surrounding mineral phases (particularly Si, Fe, or Mg rich phases) in a process known as beam mixing[26,31], leading to inaccurate Fo-content results. Ideally, measurements should be limited to individual grains to reduce the effects of beam mixing; however, tool marks left by the abrasion bit obscure grain extents, making visual identification of grain boundaries unreliable[32] and hindering accurate mineral chemistry. Previously, the effects of beam mixing on PIXL measurements have been reduced through processes such as mineral stripping[26] and compositional deconvolution into mineral endmembers[31]. These methods require significant user input[31], making their general application difficult and subject to user error, limiting their application.

Here, we extended the diffraction mapping technique developed by Orenstein et al. (2024)[23] and combined it with data from the Mineral Identification by SToichiometry (MIST) algorithm[33] to identify and investigate elemental variations across populations of olivine crystals with reduced contamination from surrounding minerals. This combination of PIXL elemental and diffraction data allows us to accurately map the Fo-content without contamination from surrounding material in abrasion patches collected during the first 1153 sols of the mission, revealing distinct olivine populations for each of *Perseverance's* science campaigns.

Perseverance's traverse

Perseverance performed four science campaigns during the first 1153 sols of the Mars 2020 mission; the crater floor campaign (sols 100-379)[34], the fan front campaign (sols 410-709)[35], the upper fan campaign (sols 708-910)[36-38], and the Margin Unit campaign (beginning sol 910)[36,39], with crystalline olivine observed in abrasion patches in all campaigns except for the fan front (Fig. 1). During these campaigns SuperCam LIBS detected olivine Fo-content between ~50 and ~80[40]. This spans a similar Fo-content range from Martian meteorite classes (except for nakhlites and augite-rich shergottites)[40,41], orbital measurements conducted prior to landing (Fo-content between 60 and 70)[2], and results from the *Curiosity* rover at Gale crater where Fo-content between 60 and 72 was determined for fluvio-lacustrine samples and between 54 and 60 for igneous samples[42].

During the crater floor campaign, observations of the Máaz formation (abrasion targets: Guillaumes, Bellegarde, Montpezat and Alfalfa) revealed interlocking submillimetric to millimetric plagioclase and pyroxene, in addition to olivine altered to Fe-rich serpentine, interpreted as a lava flow that underwent aqueous alteration[24,43-47]. In the Séítah formation (abrasion targets: Garde, Dourbes and Quartier), coarse-grained pyroxene enclosing mm-scale olivine grains were interpreted as an igneous cumulate that later underwent aqueous alteration[20,26,43]. Olivine Fo-content values between 47 and 73 from PIXL and SuperCam data are consistent with chemical disequilibrium between olivine and the melt, further supporting the cumulate interpretation[20,48,40]. Recent investigations suggest that Quartier represents an evolution of the igneous body (Séítah formation) that was intruded as a shallow sill between lava flows of the Séítah and Máaz formations rather than being a member of the Séítah formation[49].

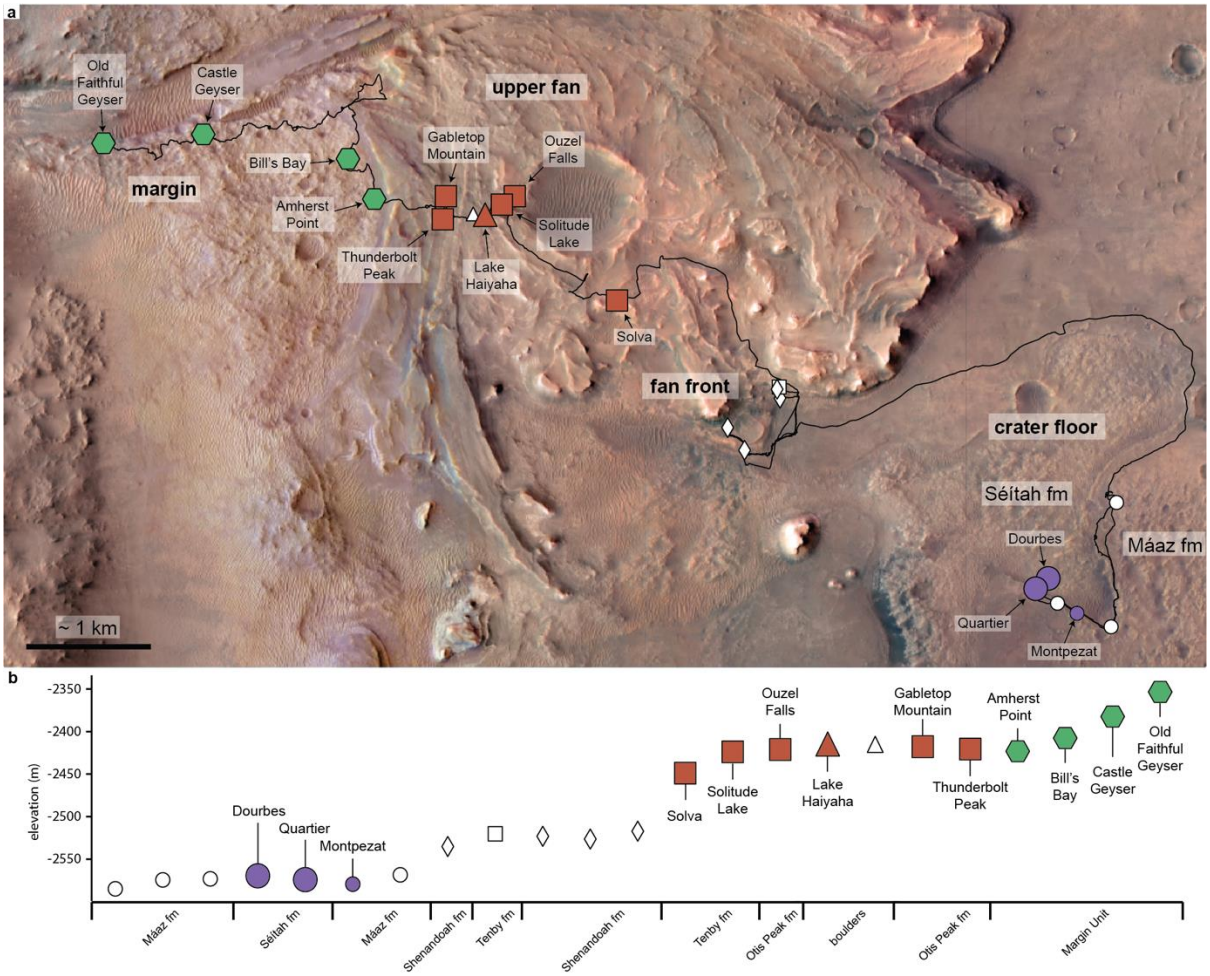

Figure 1. (a) Orbital context image showing the *Perseverance* rover traverse and locations of monocrystalline olivine in abrasion targets in Jezero crater. See Table S4 for image source. (b) Elevations and geologic units for the studied abrasion patches. Circles correspond to the crater floor, diamonds to the fan front, squares to the upper fan, triangles to float boulders in the upper fan and hexagons to the Margin Unit. Larger coloured markers correspond to abrasions with olivine identified by MIST in spatially coherent monocrystalline regions, smaller coloured markers correspond to abrasions without MIST identified olivine in spatially coherent monocrystalline regions (Table 1). A single colour is given to each science campaign analysed in this study. Smaller white markers correspond to abrasions without any detected stoichiometric olivine. During the crater floor campaign, the rover traversed the boundary between the Máaz and Séítah formations (a).

The upper fan campaign includes the Tenby and Otis Peak formations. The Tenby formation (abrasion targets: Solva, Solitude Lake) consists of medium-grained mafic sandstone with possible Fe-Mg carbonate cements[50]. The overlying conglomeritic Otis Peak formation (abrasion targets: Ouzel Falls, Gabletop Mountain, and Thunderbolt Peak) hosts millimetric clasts of olivine modified by a suite of alteration phases[51], and sandstones with sedimentary structures consistent with fluvial deposition[38,50]. Throughout both the fan front and upper fan campaigns SuperCam detected a wide spread of olivine compositions (Fo-content: 52 - 78)[40].

A suite of compositionally distinct float boulders lie atop the Otis Peak formation; their origin and transport mechanism(s) to their present location are not clear. Two classes of boulders have been described[52]: (1) Olivine-rich, exemplified by the Falcon Lake boulder (abrasion target: Lake Haiyaha), which contains mm-scale olivine grains in textures reminscent of an igneous cumulate[53,54]; and (2) Pyroxene-rich, exemplified by the Mount Meeker boulder (abrasion target: Dragon's Egg), which is notably rich in aluminous low-Ca-pyroxene[55]. PIXL results indicate that olivine in the olivine-rich boulders is far more magnesian (Fo-content between 70 and 80)[54] than other targets, while both PIXL and SuperCam results show a narrower compositional spread than other targets, consistent with a distinct, potentially more primitive source[40,53,54].

At Mandu Wall, *Perseverance* crossed a contact between the Margin Unit and the western sedimentary fan, which overlies it[39]. The Amherst Point abrasion target in the Hans Amundsen Memorial workspace in the eastern portion of the Margin Unit showed millimetric olivine grains variably altered to carbonate and rimmed by a low-Fe-Mg silicate, and intergranular space predominantly filled with Fe/Mg carbonate and silica[56-58]. *Perseverance* investigated an additional olivine-bearing abrasion target (Bill's Bay) of broadly similar texture and composition, before moving from the Eastern to Western Margin Unit. Two abrasions were created in the Western Margin Unit; Castle Geyser and Old Faithful Geyser. SuperCam results from the Margin Unit show a similar Fo-content range to the Séitah formation and to results from the fan front and upper fan campaigns[40].

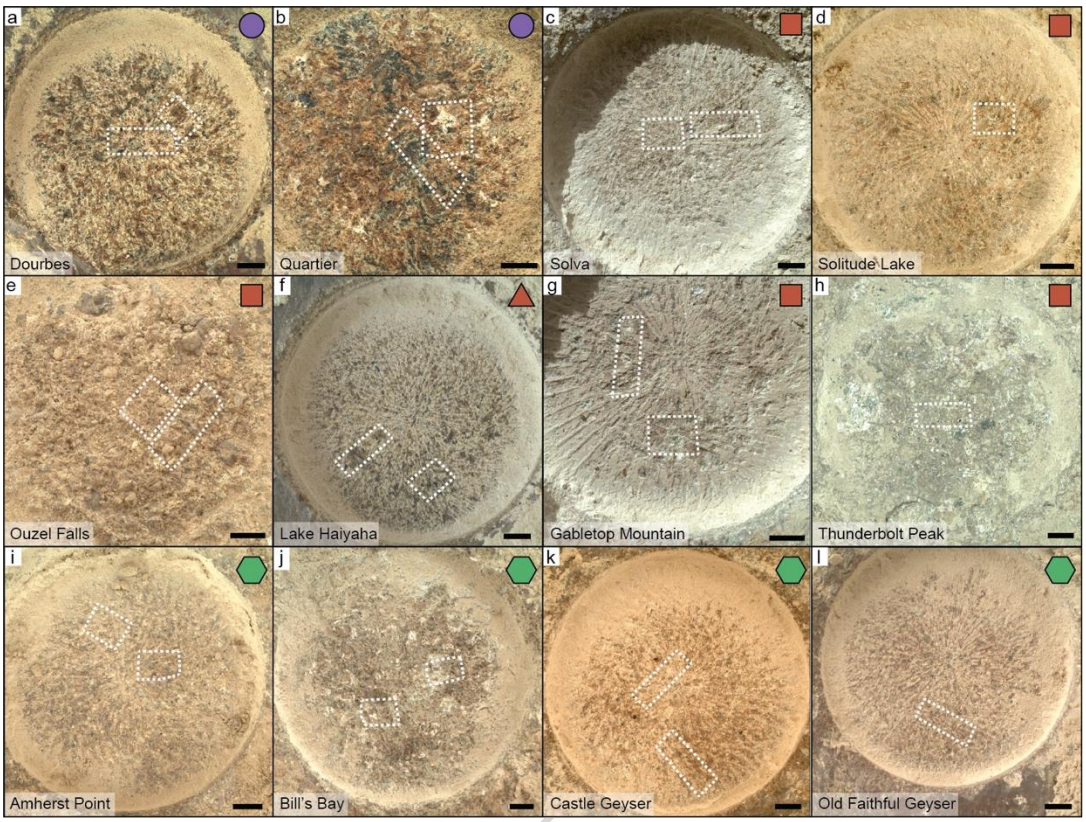

Figure 2. WATSON images of abrasion patches with PIXL scan footprints in dashed white areas for the scans included in this study; a = Dourbes, b = Quartier, c = Solva, d = Solitude Lake, e = Ouzel falls, f = Lake Haiyaha, g = Gabletop Mountain, h = Thunderbolt peak, i = Amherst Point, j = Bill's Bay, k = Castle Geyser, l = Old Faithful Geyser. Scalebar in each panel is approximately 5 mm. Coloured markers in the upper right of each panel correspond to the campaign location in Fig. 1. See Table S4 for image sources.

Monocrystalline olivine chemistry

The MIST algorithm[33] can be used to accurately measure and map the Fo-content of olivine in PIXL scans (Fig. 3a)[59]. Beam mixing[26,31], however, can result in contaminated Fo-content calculations. To reduce this effect, we used PIXL diffraction data (Fig. 3b) and extended the diffraction mapping technique developed by Orenstein et al., (2024)[23] to create constrained spatially coherent monocrystalline regions (Fig. 3c) that isolate individual crystals. Combining these monocrystalline regions with data from the MIST algorithm ensures only olivine detected within these discrete mineral crystals are included in the analysis. This results in spatially

mapped Fo-content from within individual mineral grains with reduced contamination from surrounding minerals (Fig. 3d). Comparison with context images (Fig. 3e, f) highlight the difficulty in identifying individual grains from images alone. Individual beam locations in the monocrystalline olivine maps (Fig. 3d) arise from one of two scenarios; i) where olivine was identified in a single beam location within a larger monocrystalline region or ii) where only one beam location remains after the monocrystalline region was spatially constrained. Using this method, monocrystalline olivine was identified in the crater floor, upper fan, and Margin Unit campaigns. No monocrystalline olivine was detected in the Máaz formation of the crater floor[60] or in the Shenandoah formation of the fan front (see Supplementary Information). Table 1 shows summary statistics for olivine detections.

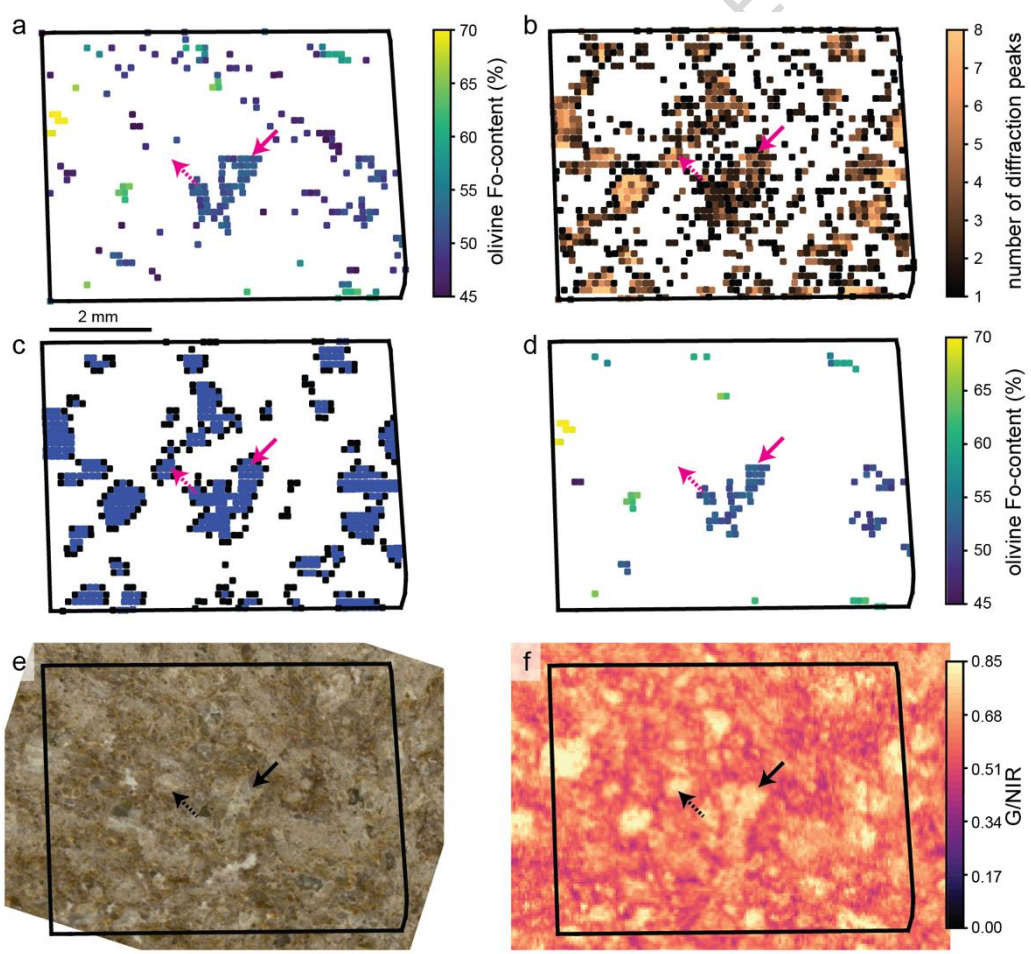

Figure 3. Combining MIST stoichiometic olivine and spatially coherent monocrystalline mapping to remove beam mixing effects and increase the Fo-content accuracy. (a) PIXL beam locations for a PIXL scan on the Solva abrasion patch (Fig. 1, 2c, S5) with compositions of stoichiometric olivine, as identified with the MIST algorithm[33,59]. Arrows point to a large olivine grain discernable in context imagery. (b) The number of diffraction peaks detected at each beam location. (c) Spatially coherent monocrystalline regions (black) and their spatially constrained interior regions (blue). (d) Compositions of monocrystalline stoichiometric olivine in the spatially constrained monocrystalline regions, as calculated with the MIST algorithm. (e) PIXL scan outline overlaid on a colourized ACI image[61] of the abrasion patch. Colourization image processing credit: NASA/JPL-Caltech/MSSS/S. Sharma. (f) PIXL MCC Green (530 nm)/IR (735 nm) image[62].

Table 1. Olivine distributions within spatially constrained coherent monocrystalline regions and all MIST identified olivine for the abrasion targets with MIST identified olivine up to mission sol 1153. ^ indicates no olivine in spatially constrained coherent monocrystalline regions identified in the abrasion; # denotes the abrasion was on a boulder.

Campaign (formation/unit)	Abrasion target (total no. of beam locations)	Spatially coherent olivine			MIST identified olivine		
		Range olivine Fo-content (%)	Mean (SD) olivine Fo-content (%)	No. beam locations (% of all beam locations)	Range olivine Fo-content (%)	Mean (SD) olivine Fo-content (%)	No. beam locations
crater floor (Séítah)	Dourbes (5670)	43.56-58.06	53.46(1.29)	1435 (25.3%)	43.56-58.06	53.41(1.37)	1621
crater floor (Séítah)	Quartier (6582)	37.75-48.07	45.48(1.32)	157 (2.4%)	36.75-48.07	44.79(2.29)	251
crater floor (Máaz)	Montpezat^ (2337)	-	-	0 (-)	15.69-20.96	19.02(2.90)	3
upper fan (Tenby)	Solva (5670)	44.02-71.68	55.35(6.58)	149 (2.6%)	42.19-71.68	52.41(6.25)	349
upper fan (Tenby)	Solitude Lake (2337)	58.91-62.63	61.01(1.12)	9 (0.5%)	45.03-62.63	52.73(3.96)	75
upper fan (Otis Peak)	Ouzel Falls (5670)	49.49-68.96	60.09(5.62)	22 (0.4%)	32.34-68.96	60.14(6.71)	81
upper fan (N/A)	Lake Haiyaha# (5188)	66.44-78.86	74.47(1.30)	1932 (37.3%)	54.55-78.86	74.33(1.53)	2259
upper fan (Otis Peak)	Gabletop Mountain (5188)	51.07-68.74	59.92(6.68)	19 (0.4%)	41.43-68.74	52.70(6.11)	108
upper fan (Otis Peak)	Thunderbolt Peak (2581)	49.60-65.77	57.77(5.07)	33 (1.3%)	35.47-68.15	55.29(6.37)	92
margin (Margin)	Amherst Point (4674)	42.57-56.92	50.76(2.48)	257 (5.5%)	31.74-58.07	49.66(3.29)	533
margin (Margin)	Bill's Bay (4674)	41.33-58.99	53.70(4.53)	50 (1.1%)	26.40-64.20	50.60(6.35)	160
margin (Margin)	Castle Geyser (6666)	45.06-57.22	52.56(2.68)	71 (1.1%)	43.73-60.94	51.68(3.05)	372
margin (Margin)	Old Faithful Geyser (2581)	47.61-60.53	56.36(3.52)	64 (2.5%)	44.23-62.48	54.59(3.59)	196

Monocrystalline olivine was plotted on a sina plot[63,64] which shows the distribution of data by plotting individual data points with a width proportional to the density of points. Inspection of

the sina plot of monocrystalline olivine regions reveals several distinct chemical populations encountered across the entire traverse (Fig. 4). Dourbes and Quartier (crater floor[34]; Figs. S3, S4), together with Lake Haiyaha (representing a boulder in float in the upper fan[54]; Fig. S8) all have a narrow distribution of Fo-content (low standard deviations), with Quartier the most fayalitic and Lake Haiyaha the most forsteritic population investigated here. The upper fan abrasion targets represent the greatest Fo-content distributions, with the Hartigan's dip test of unimodality[65] revealing evidence of multiple Fo populations in Gabletop Mountain and Thunderbolt Peak with modal centres at Fo-content of 52.3, 57.6, and 65.7 / 64.8 (Figs. 4, S9, S10, Table S2) representing distinct clusters of adjacent beam locations with similar Fo-content. Qualitatively, three distinct groupings can also be seen in Solva's Fo-content distribution, which similarly correspond to different clasts in the mapped area (Fig. S4). In the Margin Unit, Amherst Point, Bill's Bay, Castle Geyser and Old Faithful Geyser have similar Fo-content distributions. A lithological distinction between the eastern and western regions of the Margin Unit[66-68] is not supported from SuperCam elemental and textural analyses[69] or by similar Fo-content values reported here (east mean = 51.2, SD = 3.1; west mean = 54.4, SD = 3.6), however a slight trend towards higher Fo-content is observed from east to west possibly indicating a different alteration history.

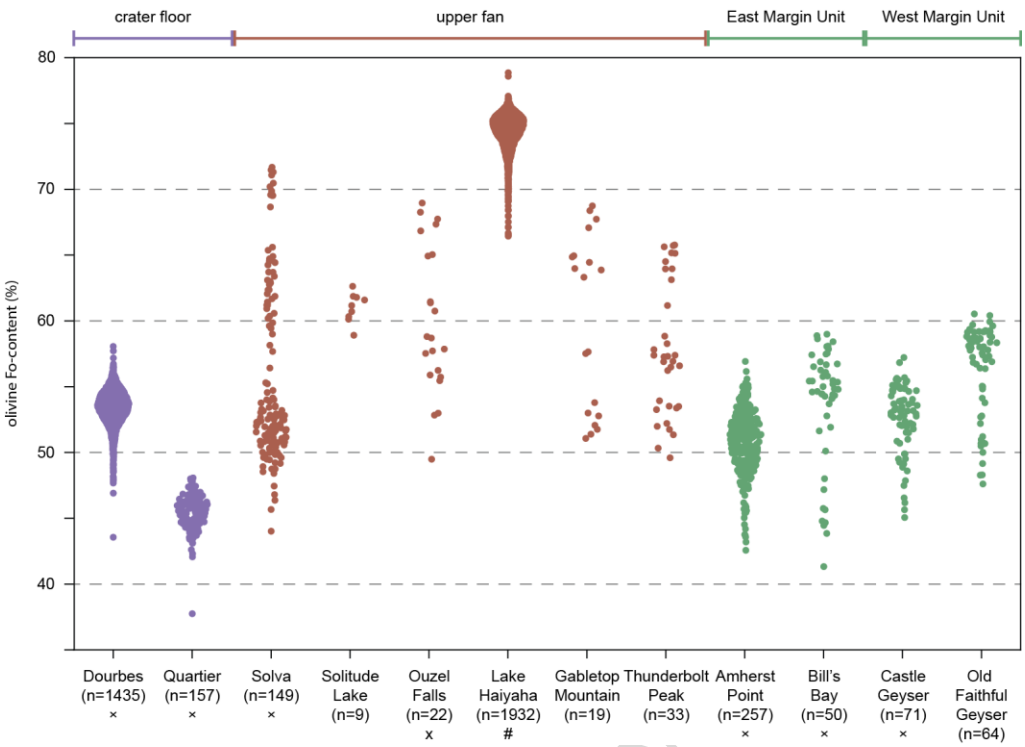

Figure 4. The forsterite content (Fo-content) for MIST olivine beam locations contained within spatially constrained coherent monocrystalline regions by abrasion target. # indicates abrasions created on a boulder and × corresponds to abrasion targets where a core sample was collected for Mars Sample Return.

Comparison to SuperCam LIBS

PIXL and SuperCam have detected olivine throughout *Perseverance's* traverse (see section "*Perseverance's* traverse"). Fo-content analysis from the two instruments often results in some discrepancies[48]. SuperCam overestimates Fo-content by ~3 for the olivine standard in their calibration suite due to underestimation of FeO_T and overestimation of SiO_2 causing some olivine to be incorrectly classified[48]. PIXL has quantification uncertainties for the olivine containing oxides (FeO_T, MgO, SiO_2) of up to 5% leading to similar Fo-content uncertainties[70].

Analysis of the spatially resolved olivine data (Fig. 3, S3-S14) shows that olivine is not typically found in large areas but found in relatively small grains under 1 mm in length. The relatively small beam size of PIXL combined with contiguous mapping allow us to isolate these individual

grains using the combination of elemental and structural information and then to discard the edges of the grains, reducing the influence from the surrounding material. This type of analysis is not possible without contiguous mapping capabilities. SuperCam LIBS analyses are not contiguous and therefore individual grains cannot be isolated for analysis. Furthermore, the SuperCam beam is approximately twice the size of the PIXL beam[16,18], increasing the likelihood of contamination from the surrounding material. In the case of the Lake Haiyaha abrasion target (Fig. S8), both PIXL and SuperCam provide similar Fo-content values on a relatively large continuous olivine grain[40,53,54]. Therefore, we interpret that discrepancies in Fo-content between PIXL and SuperCam are largely due to beam mixing effects and different analysis regions (e.g. Fig. S3, S8), with quantification uncertainties playing a minor role.

Primary igneous versus sedimentary clastic olivine

The Dourbes and Quartier abrasion targets on the crater floor yield tightly distributed Fo-content populations (SD = 1.3, 1.4), consistent with in-place igneous cumulates that cooled from a single melt[20,49,71]. Similarly, we observed a very tight Fo-content distribution (SD = 1.3) in the Falcon Lake boulder (Lake Haiyaha abrasion target) with most olivine contained within large crystals (Fig. S8)[59].

In contrast to the tight Fo-content distributions of the olivine cumulates, the abrasion targets of the clastic upper fan likely represent multiple chemically distinct olivine sources. As determined from the Gaussian mixing model (supplementary material), the most forsteritic populations for these two upper fan abrasion targets have modal Fo-content values of 65.7 and 64.8 respectively (Table S2). This is significantly higher than the Fo-content of the crater floor suggesting a different source, possibly the forsteritic olivine- and carbonate-rich western watershed[2,4,12,72] which fed Jezero crater via Neretva Vallis. As *Perseverance* traverses out of Jezero crater, it may encounter the sources of high Fo-content olivine for the clastic rocks and float boulders examined in the upper fan.

Compared to the upper fan, the relatively narrow spread of Fo-content in the Margin Unit olivine indicates less chemical diversity, indicating that if the Margin Unit is sedimentary, it was sourced

from different material than the upper fan. The unimodal distribution of Margin Unit Fo-content populations (Table S2; mean = 52.19, SD = 3.57) closely resembles the Dourbes igneous cumulate (mean = 53.46, SD = 1.29), suggesting similar igneous origins, possibly from a shared magmatic event. The greater spread of Margin Unit Fo-content compared to Dourbes could be explained by (i) zonation effects, (ii) an increased contribution of fluorescence from additional phases[26,31], (iii) post emplacement alteration, and/or (iv) primary chemical heterogeneity in a melt.

Zonation of olivine crystals can increase Fo-content spreads. In olivine-phyric shergottites, Fe-Mg zonation is mostly seen as 100-200 micron thin, Fe-rich rims around mm-sized, more Mg-rich homogenous cores (e.g.[73,74]). We found no clear evidence for zonation in the monocrystalline olivine regions studied (Figs. S3-S14) and by analogy with shergottite 'megacrysts' the signals analysed by PIXL would be dominated by core regions. Due to the strict MIST requirements for olivine identification[33] and because the edges of the monocrystalline regions were constrained to reduce the fluorescence contribution from additional phases (Fig. 3), we conclude that beam mixing effects are unlikely to be the cause of the increased Fo-content diversity in the Margin Unit.

Preferential dissolution of low Fo-content olivine, predicted by modelling performed under Martian surface conditions[75], can result in a shift towards higher overall Fo-content with less low Fo-content olivine, seen most clearly in the long tails towards low Fo-content in Bill's Bay and Old Faithful Geyser (Fig. 4). Further alteration of high Fo-content olivine results in silica-rich phases and clay phases[76] which would no longer meet the requirements for MIST identification[33]. Therefore, we suggest that olivine in the Margin Unit likely originates from a single igneous source, similar to the Dourbes abrasion target on the crater floor, but which has experienced a greater degree of aqueous alteration. These observations, in combination with the results from the Hartigan's dip test of unimodality, suggest that the variation in Fo-content in the upper fan is more likely to represent multiple sources of olivine rather than an aqueously altered olivine from a single source.

Using our novel technique combining spatial and chemical information, we are able to identify distinct chemical populations of olivine with less uncertainty than chemical data alone, allowing for inferences to be made concerning origin and emplacement. We find that in the igneous crater floor and in the sedimentary upper fan Fo-content variations are consistent with the differing emplacement mechanisms proposed for these units. The results presented here indicate that the analysed portions of the Margin Unit likely represent an altered igneous cumulate rather than being sedimentary.

Methods

Creating spatially coherent monocrystalline regions

Diffraction peaks identified in PIXL spectra using a t-test across the count values in each of PIXL's two detectors, for every energy, result in a list of diffraction peaks at energies that can be visualised on an abrasion patch as beam locations containing diffraction[77] (Fig. 3b). The diffraction is partitioned into monocrystalline regions using the energy-dispersive Bragg equation and PIXL's beam geometry[23].

Monocrystalline regions are grouped in energy but do not incorporate spatial information[23]. Therefore, to interrogate spatially coherent single crystals, spatial information needs to be incorporated which we implement in the following steps. Firstly, for each beam location, the distance to its eight nearest neighbours are calculated. For a perfect grid, this encompasses the closest beam locations in the orthogonal and diagonal directions. To filter out spatially incoherent beam locations (i.e., diffraction that is isolated to one beam location), we remove all beam locations that are not adjacent to at least two out of the nearest eight neighbours. The smallest monocrystalline region is therefore three beam locations. If the energy dependent beam size[78] is more than 1.5 times the average map spacing, then the minimum size for a monocrystalline region is increased to four. All beam locations contained within overlapping spatially coherent monocrystalline regions were then flattened through energy space. To reduce beam mixing effects[26,31] semi-isolated beam locations at the edges of each coherent

monocrystalline region where a beam location did not have three of the four nearest neighbours (Fig. 3c, black) contained within the spatially coherent monocrystalline region were removed leaving the spatially constrained interiors (Fig. 3c, blue). Three of the four nearest neighbours were selected as any less than three increases the likelihood of regions outside of the monocrystalline region being included in the analysis.

Stoichiometric filtering for olivine

The Mineral Identification by SToichiometry (MIST) algorithm is a rules-based classification model used to identify mineral endmembers in high-resolution geochemical data[33]. MIST can identify minerals where the surface exposure is larger than PIXL's energy dependent X-ray spot size of ~120 μm (measured at ~8 keV[18,78]) and is ideally implemented on data representing single mineral phases[59], such as the monocrystalline regions reported here. The MIST algorithm is able to detect olivine with high confidence across all data considered here[59].

Beam locations were obtained from PIXLISE[79] (an open source software tool for visualising PIXL data) for areas identified by MIST as stoichiometric olivine endmembers forsterite or fayalite. MIST uses normalized elemental data, so prior to inputting PIXL data into MIST, locations with oxide totals of less than 85% were excluded from the analysis, as these beam locations may contain significant amounts of non-quantified elements present below PIXL's detectable limit[26]. Instrument effects can also cause overestimation of elemental abundances[70,80] and so beam locations with oxide totals of greater than 105% were also removed from the analysis. Of the total MIST stoichiometric olivine, 4.3% has quantified totals outside this range. Of the MIST stoichiometric olivine within spatially coherent monocrystalline regions, 1.1% of beam locations had quantified totals outside of this range, consisting of 0.1% of crater floor beam locations, 3.3% of upper fan beam locations, 5.9% of Margin Unit beam locations, and 0.5% in the Lake Haiyaha boulder. Remaining spatially coherent monocrystalline regions containing MIST olivine were then selected for analysis (Fig. 3d).

MIST was given oxide abundances corrected for the effects of diffraction and surface roughness using PIXLISE v4 expressions[24], before the abundances were normalised and the olivine forsterite content was calculated. The MIST results here have also had any SO_3 and Cl determined to be allochthonous to the rock (i.e., from dust)[81-83] removed before normalization[59]. We display the Fo-content per abrasion patch as a sina plot[63,64] in Fig. 4 allowing for a visual representation of the olivine distribution and density for each target.

Image registration

MCC, ACI, WATSON, and RMI images were aligned with an affine transform in a multi-stage control point image registration routine implemented in Matlab[84]. In the first stage, three or more large features were selected to obtain the approximate relative orientation of the images. Subsequent stages focused on smaller features, with an increasing number of control points. At least five control points were used in the final stage.

Data availability

Data available at the NASA Planetary Data System https://pds.nasa.gov/.

Code availability

Code used in this manuscript is available at https://github.com/bjorens/PIXL_spatially_coherent_monocrystalline_regions/

Competing interests

The authors declare no competing interests.

Acknowledgements

This research was supported by Australian Research Council grant DE210100205. The research was carried out in part at the Jet Propulsion Laboratory, California Institute of Technology, under a contract with the National Aeronautics and Space Administration (80NM0018D0004). E.A.C.

thanks the Natural Sciences and Engineering Research Council of Canada (grant #RGPIN-2023-03413) and the Canadian Space Agency (grant #22EXPCOI4) for their support. We acknowledge the members of the Mars 2020 team that performed mission operations and thank Christoph Schrank, Olivier Beysacc, Nicolas Mangold, Elise Clavé, and the SuperCam team for feedback that improved the manuscript. We also thank Jesper Henneke and David Arge Klevang for their assistance in aligning PIXL footprints to ACI and MCC images.

References

1 Werner, S. C. The early martian evolution—Constraints from basin formation ages. *Icarus* **195**, 45-60, doi:https://doi.org/10.1016/j.icarus.2007.12.008 (2008).

2 Hoefen, T. M. *et al.* Discovery of Olivine in the Nili Fossae Region of Mars. *Science* **302**, 627-630, doi:doi:10.1126/science.1089647 (2003).

3 Hamilton, V. E. & Christensen, P. R. Evidence for extensive, olivine-rich bedrock on Mars. *Geology* **33**, 433-436, doi:10.1130/g21258.1 (2005).

4 Ehlmann, B. L. *et al.* Orbital Identification of Carbonate-Bearing Rocks on Mars. *Science* **322**, 1828-1832, doi:doi:10.1126/science.1164759 (2008).

5 Mustard, J. F. *et al.* Mineralogy of the Nili Fossae region with OMEGA/Mars Express data: 1. Ancient impact melt in the Isidis Basin and implications for the transition from the Noachian to Hesperian. *Journal of Geophysical Research: Planets* **112**, doi:https://doi.org/10.1029/2006JE002834 (2007).

6 Mustard, J. F. *et al.* Composition, Morphology, and Stratigraphy of Noachian Crust around the Isidis basin. *Journal of Geophysical Research: Planets* **114**, doi:https://doi.org/10.1029/2009JE003349 (2009).

7 Tornabene, L. L. *et al.* Surface and crater-exposed lithologic units of the Isidis Basin as mapped by coanalysis of THEMIS and TES derived data products. *Journal of Geophysical Research: Planets* **113**, doi:https://doi.org/10.1029/2007JE002988 (2008).

8 Rogers, A. D., Warner, N. H., Golombek, M. P., Head III, J. W. & Cowart, J. C. Areally Extensive Surface Bedrock Exposures on Mars: Many Are Clastic Rocks, Not Lavas. *Geophysical Research Letters* **45**, 1767-1777, doi:https://doi.org/10.1002/2018GL077030 (2018).

9 Kremer, C. H., Mustard, J. F. & Bramble, M. S. A widespread olivine-rich ash deposit on Mars. *Geology* **47**, 677-681, doi:10.1130/g45563.1 (2019).

10 Ruff, S. W., Hamilton, V. E., Rogers, A. D., Edwards, C. S. & Horgan, B. H. N. Olivine and carbonate-rich bedrock in Gusev crater and the Nili Fossae region of Mars may be altered ignimbrite deposits. *Icarus* **380**, 114974, doi:https://doi.org/10.1016/j.icarus.2022.114974 (2022).

11 Brown, A. J., Viviano, C. E. & Goudge, T. A. Olivine-Carbonate Mineralogy of the Jezero Crater Region. *Journal of Geophysical Research: Planets* **125**, e2019JE006011, doi:https://doi.org/10.1029/2019JE006011 (2020).

12 Goudge, T. A., Mustard, J. F., Head, J. W., Fassett, C. I. & Wiseman, S. M. Assessing the mineralogy of the watershed and fan deposits of the Jezero crater paleolake system, Mars.

Journal of Geophysical Research: Planets **120**, 775-808, doi:https://doi.org/10.1002/2014JE004782 (2015).

13 Tarnas, J. D. *et al.* Characteristics, Origins, and Biosignature Preservation Potential of Carbonate-Bearing Rocks Within and Outside of Jezero Crater. *Journal of Geophysical Research: Planets* **126**, e2021JE006898, doi:https://doi.org/10.1029/2021JE006898 (2021).

14 Viviano, C. E., Moersch, J. E. & McSween, H. Y. Implications for early hydrothermal environments on Mars through the spectral evidence for carbonation and chloritization reactions in the Nili Fossae region. *Journal of Geophysical Research: Planets* **118**, 1858-1872, doi:https://doi.org/10.1002/jgre.20141 (2013).

15 Horgan, B. H. N., Anderson, R. B., Dromart, G., Amador, E. S. & Rice, M. S. The mineral diversity of Jezero crater: Evidence for possible lacustrine carbonates on Mars. *Icarus* **339**, 113526, doi:https://doi.org/10.1016/j.icarus.2019.113526 (2020).

16 Maurice, S. *et al.* The SuperCam Instrument Suite on the Mars 2020 Rover: Science Objectives and Mast-Unit Description. *Space Science Reviews* **217**, 47, doi:10.1007/s11214-021-00807-w (2021).

17 Wiens, R. C. *et al.* The SuperCam Instrument Suite on the NASA Mars 2020 Rover: Body Unit and Combined System Tests. *Space Science Reviews* **217**, 4, doi:10.1007/s11214-020-00777-5 (2020).

18 Allwood, A. C. *et al.* PIXL: Planetary Instrument for X-Ray Lithochemistry. *Space Science Reviews* **216**, 134, doi:10.1007/s11214-020-00767-7 (2020).

19 Moeller, R. C. *et al.* The Sampling and Caching Subsystem (SCS) for the Scientific Exploration of Jezero Crater by the Mars 2020 Perseverance Rover. *Space Science Reviews* **217**, 5, doi:10.1007/s11214-020-00783-7 (2020).

20 Liu, Y. *et al.* An olivine cumulate outcrop on the floor of Jezero crater, Mars. *Science* **377**, 1513-1519, doi:doi:10.1126/science.abo2756 (2022).

21 Schofield, R. E. *et al.* in *Lunar and Planetary Science XLVIII* 2955 (Texas, USA, 2017).

22 Jones, M. W. M. *et al.* In situ crystallographic mapping constrains sulfate precipitation and timing in Jezero crater, Mars. *Science Advances* **11**, eadt3048, doi:doi:10.1126/sciadv.adt3048 (2025).

23 Orenstein, B. J. *et al.* In-situ mapping of monocrystalline regions on Mars. *Icarus* **420**, 116202, doi:https://doi.org/10.1016/j.icarus.2024.116202 (2024).

24 Schmidt, M. E. *et al.* Diverse and highly differentiated lava suite in Jezero crater, Mars: Constraints on intracrustal magmatism revealed by Mars 2020 PIXL. *Science Advances* **11**, eadr2613, doi:10.1126/sciadv.adr2613 (2025).

25 Schrank, C. E., Jones, M. W. M., Howard, D. L., Berger, A. & Herwegh, M. Micro-scale structural and chemical characterisation of deformed rocks with simultaneous in-situ synchrotron X-ray fluorescence and backscatter diffraction mapping. *Chemical Geology* **645**, 121886, doi:https://doi.org/10.1016/j.chemgeo.2023.121886 (2024).

26 Tice, M. M. *et al.* Alteration history of Séitah formation rocks inferred by PIXL x-ray fluorescence, x-ray diffraction, and multispectral imaging on Mars. *Science Advances* **8**, eabp9084, doi:doi:10.1126/sciadv.abp9084 (2022).

27 Bhartia, R. *et al.* Perseverance's Scanning Habitable Environments with Raman and Luminescence for Organics and Chemicals (SHERLOC) Investigation. *Space Science Reviews* **217**, 58, doi:10.1007/s11214-021-00812-z (2021).

28 Maki, J. N. *et al.* The Mars 2020 Engineering Cameras and Microphone on the Perseverance Rover: A Next-Generation Imaging System for Mars Exploration. *Space Science Reviews* **216**, 137, doi:10.1007/s11214-020-00765-9 (2020).

29 Roeder, P. L. & Emslie, R. F. Olivine-liquid equilibrium. *Contributions to Mineralogy and Petrology* **29**, 275-289, doi:10.1007/BF00371276 (1970).

30 Stöffler, D. & Knöll, H.-D. in *In: Lunar Science Conference, 8th, Houston, Tex., March 14-18, 1977, Proceedings. Volume 2.(A78-41551 18-91) New York, Pergamon Press, Inc., 1977, p. 1849-1867. Research supported by the Deutsche Forschungsgemeinschaft.* 1849-1867.

31 Kizovski, T. V. *et al.* Fe-phosphates in Jezero Crater as evidence for an ancient habitable environment on Mars. *Nature Communications* **16**, 6470, doi:10.1038/s41467-025-60026-7 (2025).

32 Henley, T. L. J. *In Situ Investigation of the Martian Surface: Quantification of Dust Coverages in Gale crater and Abrasion Marks in Jezero crater* Master of Science thesis, Brock University, (2023).

33 Siebach, K. L., Moreland, E. L., Costin, G. & Jiang, Y. MIST: An online tool automating mineral identification by stoichiometry. *Computers & Geosciences* **206**, 106021, doi:https://doi.org/10.1016/j.cageo.2025.106021 (2026).

34 Sun, V. Z. *et al.* Overview and Results From the Mars 2020 Perseverance Rover's First Science Campaign on the Jezero Crater Floor. *Journal of Geophysical Research: Planets* **128**, e2022JE007613, doi:https://doi.org/10.1029/2022JE007613 (2023).

35 Stack, K. M. *et al.* Sedimentology and Stratigraphy of the Shenandoah Formation, Western Fan, Jezero Crater, Mars. *Journal of Geophysical Research: Planets* **129**, e2023JE008187, doi:https://doi.org/10.1029/2023JE008187 (2024).

36 Herd, C. D. K. *et al.* Sampling Mars: Geologic context and preliminary characterization of samples collected by the NASA Mars 2020 Perseverance Rover Mission. *Proceedings of the National Academy of Sciences* **122**, e2404255121, doi:doi:10.1073/pnas.2404255121 (2025).

37 Huang, W. *et al.* Mineralogical Diversity in the Upper Fan Campaign at Jezero Crater, Mars. *Journal of Geophysical Research: Planets* **130**, e2024JE008750, doi:https://doi.org/10.1029/2024JE008750 (2025).

38 Nachon, M. *et al.* in *55th Lunar and Planetary Science Conference.* 2317.

39 Horgan, B. *et al.* in *55th Lunar and Planetary Science Conference.* 2624.

40 Udry, A. *et al.* Igneous processes at Jezero Crater and comparison to other Martian igneous compositions. (2024).

41 Udry, A. *et al.* What Martian Meteorites Reveal About the Interior and Surface of Mars. *Journal of Geophysical Research: Planets* **125**, e2020JE006523, doi:https://doi.org/10.1029/2020JE006523 (2020).

42 Rampe, E. B. *et al.* Mineralogy and geochemistry of sedimentary rocks and eolian sediments in Gale crater, Mars: A review after six Earth years of exploration with Curiosity. *Geochemistry* **80**, 125605, doi:https://doi.org/10.1016/j.chemer.2020.125605 (2020).

43 Farley, K. A. *et al.* Aqueously altered igneous rocks sampled on the floor of Jezero crater, Mars. *Science* **377**, eabo2196, doi:doi:10.1126/science.abo2196 (2022).

44 Horgan, B. *et al.* Mineralogy, Morphology, and Emplacement History of the Maaz Formation on the Jezero Crater Floor From Orbital and Rover Observations. *Journal of*

Geophysical Research: Planets **128**, e2022JE007612, doi:https://doi.org/10.1029/2022JE007612 (2023).

45 Udry, A. *et al.* A Mars 2020 Perseverance SuperCam Perspective on the Igneous Nature of the Máaz Formation at Jezero Crater and Link With Séítah, Mars. *Journal of Geophysical Research: Planets* **128**, e2022JE007440, doi:https://doi.org/10.1029/2022JE007440 (2023).

46 Wiens, R. C. *et al.* Compositionally and density stratified igneous terrain in Jezero crater, Mars. *Science Advances* **8**, eabo3399, doi:doi:10.1126/sciadv.abo3399 (2022).

47 Tosca, N. J. *et al.* In situ evidence for serpentinization within the Máaz formation, Jezero crater, Mars. *Science Advances* **11**, eadr8793, doi:doi:10.1126/sciadv.adr8793 (2025).

48 Beyssac, O. *et al.* Petrological Traverse of the Olivine Cumulate Séítah Formation at Jezero Crater, Mars: A Perspective From SuperCam Onboard Perseverance. *Journal of Geophysical Research: Planets* **128**, e2022JE007638, doi:https://doi.org/10.1029/2022JE007638 (2023).

49 Hernández-Montenegro, J. D. *et al.* Petrogenesis of the olivine cumulate outcrop Issole – The missing link between the Séítah and Máaz formations in Jezero crater, Mars. *Icarus* **437**, 116620, doi:https://doi.org/10.1016/j.icarus.2025.116620 (2025).

50 Siebach, K. *et al.* in *55th Lunar and Planetary Science Conference.* 2365.

51 Weiss, B. *et al.* in *55th Lunar and Planetary Science Conference.*

52 Vaughan, A. F. *et al.* The Boulder-Rich Blocky Unit of the Western Jezero Upper Fan: Discriminating Olivine and Pyroxene Compositions and Constraining Provenance. *Authorea Preprints* (2025).

53 Beyssac, O. *et al.* in *55th Lunar and Planetary Science Conference (LPSC).* (Lunar and Planetary Institute).

54 Moreland, E. *et al.* in *55th Lunar and Planetary Science Conference.* 2030.

55 Treiman, A. H. *et al.* in *55th Lunar and Planetary Science Conference.* 1283.

56 Hurowitz, J. *et al.* in *55th Lunar and Planetary Science Conference.* 2541.

57 Garczynski, B. *et al.* in *Proceedings of the 55th Lunar and Planetary Science Conference. Woodlands: Lunar and Planetary Institute.*

58 Sinclair, K. P., Catling, D. C. & Elam, W. T. in *Tenth International Conference on Mars.* 3434.

59 Moreland, E. L. *et al.* Multiple Episodes of Fluid Alteration in Jezero Crater Indicated by MIST Mineral Identifications in PIXL XRF Data From the First 1100 Sols of the Mars 2020 Mission. *Journal of Geophysical Research: Planets* **130**, e2024JE008797, doi:https://doi.org/10.1029/2024JE008797 (2025).

60 Mandon, L. *et al.* Reflectance of Jezero Crater Floor: 2. Mineralogical Interpretation. *Journal of Geophysical Research: Planets* **128**, e2022JE007450, doi:https://doi.org/10.1029/2022JE007450 (2023).

61 Sharma, S. *et al.* in *2024 IEEE Aerospace Conference.* 1-13.

62 Klevang, D. A. *et al.* Pre-flight Geometric and Optical Calibration of the Planetary Instrument for X-ray Lithochemistry (PIXL). *Space Science Reviews* **219**, 11, doi:10.1007/s11214-023-00955-1 (2023).

63 seaborn_sinaplot (github, https://github.com/mparker2/seaborn_sinaplot, 2018).

64 sinaplot: An Enhanced Chart for Simple and Truthful Representation of Single Observations over Multiple Classes v. 1.1.0 (https://cran.r-project.org/web/packages/sinaplot/index.html, 2017).

65 Hartigan, J. A. & Hartigan, P. M. The Dip Test of Unimodality. *The Annals of Statistics* **13**, 70-84 (1985).

66 Horgan, B. *et al.* in *Tenth International Conference on Mars*. 3543.

67 Jones, A. J. *et al.* in *55th Lunar and Planetary Science Conference*. 1994.

68 Randazzo, N. *et al.* in *55th Lunar and Planetary Science Conference* 2108 (The Woodlands (Texas), United States, 2024).

69 Bedford, C. *et al.* Investigating the Origin and Alteration History of the Margin Unit in Jezero Crater, Mars, with the SuperCam Instrument. *LPI Contributions* **3090**, 1946 (2025).

70 Heirwegh, C. M., Elam, W. T., O'Neil, L. P., Sinclair, K. P. & Das, A. The focused beam X-ray fluorescence elemental quantification software package PIQUANT. *Spectrochimica Acta Part B: Atomic Spectroscopy* **196**, 106520, doi:https://doi.org/10.1016/j.sab.2022.106520 (2022).

71 Treiman, A. H. *et al.* The Brac/Dourbes Olivine-Cumulate Rock, Séítah Formation, Jezero Crater Floor, Mars: Its Parent Magma, and Relation to Basalts of the Máaz Formation. *Journal of Geophysical Research: Planets* **130**, e2024JE008539, doi:https://doi.org/10.1029/2024JE008539 (2025).

72 Fassett, C. I. & Head III, J. W. Fluvial sedimentary deposits on Mars: Ancient deltas in a crater lake in the Nili Fossae region. *Geophysical Research Letters* **32**, doi:https://doi.org/10.1029/2005GL023456 (2005).

73 Barrat, J. A. *et al.* Petrology and chemistry of the Picritic Shergottite North West Africa 1068 (NWA 1068). *Geochimica et Cosmochimica Acta* **66**, 3505-3518, doi:https://doi.org/10.1016/S0016-7037(02)00934-1 (2002).

74 Basu Sarbadhikari, A., Day, J. M. D., Liu, Y., Rumble, D. & Taylor, L. A. Petrogenesis of olivine-phyric shergottite Larkman Nunatak 06319: Implications for enriched components in martian basalts. *Geochimica et Cosmochimica Acta* **73**, 2190-2214, doi:https://doi.org/10.1016/j.gca.2009.01.012 (2009).

75 Stopar, J. D., Jeffrey Taylor, G., Hamilton, V. E. & Browning, L. Kinetic model of olivine dissolution and extent of aqueous alteration on mars. *Geochimica et Cosmochimica Acta* **70**, 6136-6152, doi:https://doi.org/10.1016/j.gca.2006.07.039 (2006).

76 Dehouck, E. *et al.* Weathering of olivine under CO2 atmosphere: A martian perspective. *Geochimica et Cosmochimica Acta* **135**, 170-189, doi:https://doi.org/10.1016/j.gca.2014.03.032 (2014).

77 Wright, A. P., Nemere, P., Galvin, A., Chau, D. H. & Davidoff, S. in *Proceedings of the 28th International Conference on Intelligent User Interfaces* 91–105 (Association for Computing Machinery, Sydney, NSW, Australia, 2023).

78 Das, A. *et al.* Energy dependence of x-ray beam size produced by polycapillary x-ray optics. *X-Ray Spectrometry*, doi:10.1002/xrs.3450 (2024).

79 PIXLISE spectroscopy analysis software.

80 VanBommel, S. X-Ray Interrogation Effects in APXS and PIXL Data. *LPI Contributions* **3007**, 3044 (2024).

81 Schmidt, M. E. *et al.* Geochemical diversity in first rocks examined by the Curiosity Rover in Gale Crater: Evidence for and significance of an alkali and volatile-rich igneous source. *Journal of Geophysical Research: Planets* **119**, 64-81, doi:https://doi.org/10.1002/2013JE004481 (2014).

82 Siebach, K. L. *et al.* Sorting out compositional trends in sedimentary rocks of the Bradbury group (Aeolis Palus), Gale crater, Mars. *Journal of Geophysical Research: Planets* **122**, 295-328, doi:https://doi.org/10.1002/2016JE005195 (2017).
83 Stolper, E. M. *et al.* The Petrochemistry of Jake_M: A Martian Mugearite. *Science* **341**, 1239463, doi:doi:10.1126/science.1239463 (2013).
84 MATLAB. *Image Processing Toolbox*. (The MathWorks Inc., 2023b).

Editorial summary:
The Margin Unit of Jezero crater contains olivine with a forsterite content similar to the olivine cumulates in the crater floor, according to an approach which uses X-ray data from the Perseverance rover to analyse monocrystalline olivine composition

Peer review information:
Communications Earth and Environment thanks Elizabeth Rampe and the other, anonymous, reviewer(s) for their contribution to the peer review of this work. Primary Handling Editors: Ke Zhu and Joe Aslin. [A peer review file is available.]